Nano Research 2015, 8(3): 821–831
DOI 10.1007/s12274-014-0564-2
Research Article

ISSN 1998-0124
CN 11-5974/O4

Photoreduction of CO_2 on BiOCl nanoplates with the assistance of photoinduced oxygen vacancies

Ling Zhang, Wenzhong Wang (✉), Dong Jiang, Erping Gao, and Songmei Sun

State Key Laboratory of High Performance Ceramics and Superfine Microstructures, Shanghai Institute of Ceramics, Chinese Academy of Sciences, Shanghai 200050, China

Received: 16 June 2014
Revised: 22 July 2014
Accepted: 16 August 2014

KEYWORDS

BiOCl nanoplates,
oxygen vacancy,
photocatalytic,
CO_2 photoreduction,
defect

ABSTRACT

CO_2 photoreduction by semiconductors is of growing interest. Fabrication of oxygen-deficient surfaces is an important strategy for enhancing CO_2 photoreduction activity. However, regeneration of the oxygen vacancies in photocatalysts is still a problem since an oxygen vacancy will be filled up by the O atom from CO_2 after the dissociation process. Herein, we have fabricated highly efficient BiOCl nanoplates with photoinduced oxygen vacancies. Oxygen vacancies were easily regenerated by light irradiation due to the high oxygen atom density and low Bi–O bond energy even when the oxygen vacancies had been filled up by the O atom in the photocatalytic reactions. These oxygen vacancies not only enhanced the trapping capability for CO_2, but also enhanced the efficiency of separation of electron–hole pairs, which resulted in the photocatalytic CO_2 reduction under simulated solar light. Furthermore, the generation and recovery of the defects in the BiOCl could be realized during the photocatalytic reduction of CO_2 in water. The existence of photoinduced defects in thin BiOCl nanoplates undoubtedly leads to new possibilities for the design of solar-driven bismuth based photocatalysts.

1 Introduction

Atmospheric carbon dioxide (CO_2) is the most abundant greenhouse gas and its concentration has been monotonically growing with the increasing use of fossil fuels, and has now become a severe environmental issue. Artificial photosynthesis, which employs inexpensive semiconductor photocatalysts to convert waste CO_2 into energy-bearing carbon fuel sources (e.g. CO, CH_4 or CH_3OH) with the help of solar energy, is undoubtedly one of the most sustainable and economical ways to reduce CO_2 emissions and solve the energy crisis [1–3]. However, its reduction presents an energy-intensive challenge since CO_2 is very stable. Developing an efficient photocatalyst appears to be a promising methodology to meet the challenge, and has been a prominent quest in the conversion of CO_2 into hydrocarbon fuels. To date,

---

Address correspondence to wzwang@mail.sic.ac.cn

various photocatalysts have been developed including semiconductors, such as TiO_2 [4, 5], ZnO [6, 7], Zn_2GeO_4 [8], CdS [9, 10], $BiMO_x$ (M = W, V) [11–13] and $ALa_4Ti_4O_{15}$ (A = Ca, Sr, and Ba) [14] and organic compounds, e.g., rhenium complexes [15–17]. Various hydrocarbon products have been detected over these photocatalysts, but they still suffer from some problems. For example, low conversion efficiencies, resulting from the fast electron–hole recombination rate in the photocatalysts, is still a major barrier that needs to be overcome.

Several strategies have been proposed to solve these problems, such as inducing defect disorders on the surface of a photocatalyst. First, creation of defects greatly influences its photoactivity, because the separation efficiency of photoinduced electrons and holes is enhanced in the presence of oxygen vacancies [18]. The oxygen vacancies can be the centers for capturing photoinduced electrons during the photoreactions. Thus, photoinduced electrons in the conduction band (CB) are preferentially transferred to oxygen vacancy states rather than recombining with photoinduced holes. The direct recombination of photoinduced charge carriers can thus be effectively inhibited. Second, the oxygen vacancies can serve as surface reactive sites for CO_2 binding, with an accompanying charge transfer to CO_2 [19]. It was reported that CO_2^- species, generated as a result of electron gain by CO_2, are spontaneously dissociated into CO even in the dark on a partially oxygen depleted Cu(I)/TiO_{2-x} surface [20]. The spontaneous dissociation of CO_2^- in the dark is to a large extent associated with the surface oxygen vacancies that provide not only the electronic charge (i.e., formation of Ti^{3+}) but also the sites for the adsorption of oxygen atoms from CO_2.

According to these literature results, surface oxygen vacancies may favor the separation of carriers, CO_2 activation and dissociation on defective metal oxides. However, these oxygen vacancies will be filled by the O from CO_2 after the dissociation process. The regeneration of oxygen vacancies in the photocatalyst is therefore still a problem that needs to be solved. Thus, it is a challenging task to develop highly efficient photocatalysts with regenerable oxygen vacancies for CO_2 reduction.

In recent years, BiOCl has been reported to be an excellent semiconductor photocatalyst which exhibits outstanding performance because of its open crystalline structure. It is worth noting that a few researchers have attributed its extraordinary performance to the oxygen vacancies formed on the surface of BiOCl, which are easily induced by UV light irradiation due to the low bond energy and long bond length of the Bi–O bond [21–23]. Based on first-principles studies, it has been shown that the surface O vacancies within {001} facets have Fermi energies (E_fs) close to those of O vacancies within bulk BiOCl, due to their low surface reconstruction and bulk-like geometry [22, 23]. BiOCl with {001} facets are more stable and photoinduced electron–hole (e^-–h^+) pairs within these facets can be efficiently separated. In this regard, BiOCl nanoplates with exposed {001} facets are a noteworthy model material for the in-depth and comprehensive understanding of oxygen vacancy-dependent photocatalytic properties.

In the present study, we experimentally observed CO_2 photoreduction to CO and CH_4 using thin BiOCl nanoplates with exposed {001} facets (~75%–80% of the BiOCl surface). The as-prepared BiOCl nanoplates are very thin (~10 nm) and have a high density of surface O atoms on the {001} facets, a large number of oxygen vacancies were characterized in the BiOCl-LT samples (light-treated samples). These oxygen vacancies result in not only an enhanced trapping capability for CO_2, but also an enhanced efficiency of separation of electron–hole pairs, which resulted in the photocatalytic CO_2 reduction.

2 Experimental

2.1 Preparation of BiOCl

The chemical reagents were purchased from Shanghai Reagent Co., Ltd. (China). All the chemicals were used as received without further purification. In a typical experiment, 4 mmol of hexadecyltrimethylammonium chloride (CTAC), was dissolved in a mixed solution of 2-methoxyethanol (96 mL) and H_2O (4 mL). 4 mmol of $Bi(NO_3)_3{\cdot}5H_2O$ was added to 10 mL of ethylene glycol (EG) with stirring at room temperature. After $Bi(NO_3)_3$ was dissolved completely, it was added to the mixed solution with stirring. All the reactants were sealed in a flask and maintained at 120 °C for 5 h. After the reaction was complete, a white solid (BiOCl) was obtained. The precipitate was washed with hot deionized water and ethanol, and then dried at 60 °C for 12 h.

2.2 Preparation of light-treated BiOCl (BiOCl-LT)

In order to investigate oxygen vacancies formed in the BiOCl sample after the light irradiation, a special sample denoted as BiOCl-LT was prepared as follows: The above prepared BiOCl powder was added to a quartz tube and illuminated for 5 h by a Xe lamp (500 W, Langsheng Co., Ltd. Shanghai). The resulting grey powder was collected and washed thoroughly with deionized water and dried at 60 °C in air.

2.3 Recovery of the oxygen vacancies in the BiOCl

The BiOCl sample used in the CO_2 photocatalytic reduction was collected and thoroughly washed with deionized water and dried at 60 °C in air. The above sample was irradiated under the Xe-lamp for 5 h. The white sample turned to grey and black as for the BiOCl-LT sample.

2.4 Characterization

Samples were characterized by X-ray powder diffraction (XRD) on a Rigaku powder diffractometer. Each sample was scanned using Cu Kα radiation with an operating voltage of 30 kV and an operating current of 100 mA. A scan rate of 4°/min was employed to record the patterns in the range of 10°–70° at a step size of 0.01°. UV–visible diffuse reflectance spectra (DRS) were recorded on an UV–visible spectrophotometer (Hitachi 3010) equipped with an integrating sphere. The photoluminescence (PL) spectra were measured with a Hitachi F4600 fluorescence spectrophotometer at room temperature (excitation wavelength = 280 nm). Chemical compositions of the derived products were analyzed using X-ray photoelectron spectroscopy (XPS) analysis (Thermo Scientific ESCALAB 250). All binding energies were referenced to the C 1s peak (285 eV) arising from adventitious carbon. The morphologies and microstructures of the as-prepared samples were investigated by transmission electron microscopy (TEM, JEOL JEM-2100F). IR spectra presented in this work were recorded on a Bruker Tensor 27 spectrometer.

2.5 Photocatalytic reactions

The experiments of CO_2 photoreduction with CO_2/H_2O solution on BiOCl were carried out in a closed evacuated system. The reaction mixture was prepared by the introduction of the BiOCl powder (0.1 g) to 100 mL of deionized water in a quartz reactor equipped with a cooling system. The reactants were mixed well and deaerated by nitrogen gas. Finally, pure CO_2 gas (400 ppm) was injected into the closed reactor. A 500 W Xe lamp was used as the excitation source. The light intensity of the solar simulator was ~100 mW/cm^2 in the range 200–1,000 nm. The gaseous products of CO and CH_4 in the reactor effluent were analyzed over 8 h using a gas chromatograph (GC, Tianmei 7890) equipped with a flame ionization detector (FID). The O_2 produced in the reactor was analyzed by a GC (Tianmei 7890II) equipped with a thermal conductivity detector (TCD).

3 Results and discussion

3.1 Photocatalytic reduction of CO_2 in water

Blank reaction was first conducted with the BiOCl aqueous solution under photoillumination. Photoreduction products of CO and CH_4 were not observed in the absence of CO_2, confirming that CO_2 was indeed the carbon source. Another experiment was done by introducing CO_2 but without irradiation. Neither CH_4 nor CO was formed showing that light irradiation is the key for the reduction reaction. Representative CO and CH_4 yields over the BiOCl nanoplates as a function of irradiation time are plotted in Fig. 1(a). The BiOCl nanoplates demonstrated high selectivity to CO formation. The CO yield increased with irradiation time and reached an overall value of 8.1 μmol·g^{-1} in 8 h, which is comparable to those reported in the literature using TiO_2 with oxygen vacancy for CO_2 photoreduction (see Table S1 in the Electronic Supplementary Material (ESM)). CH_4 formation was also observed but with a lower yield (1.2 μmol·g^{-1} in 8 h). CH_4 was not detected until after 2 h of irradiation due to the preferential formation of CO. Hydrogen (H_2)

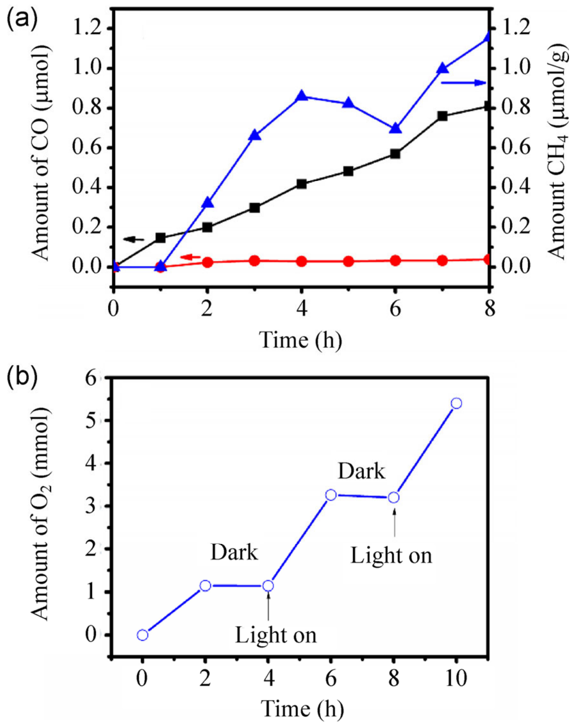

Figure 1 (a) Photocatalytic evolution of products from the BiOCl nanoplates for a period of 8 h photoillumination: (-●-) Without the CO_2, (-■-) yield of CO, (-▲-) yield of CH_4. (b) Photocatalytic evolution of O_2 from the BiOCl nanoplates.

could not be detected, indicating that the amount evolved in this work was not significant and probably all reacted with the intermediate. The evolution of O_2 from water, which is another important indicator of proton generation, is shown in Fig. 1(b) as a function of irradiation time. The plot shows the concentration of O_2 in the reactor before, during and after the photoreaction. Before the photoillumination (in the dark), the concentration of O_2 was steady. Upon photoillumination, the O_2 concentration gradually increased. When the light was turned off (the second dark period), the O_2 concentration remained essentially unchanged, but the O_2 concentration increased again when the light was turned on. The concentration of O_2 is much higher than that of CO, which means that the O_2 generation process is much faster than the CO generation process.

3.2 Recycling experiments with the BiOCl nanoplates

We tested the CO_2 photoreduction activity of the recycled BiOCl sample. Figure 2 shows that the recycled BiOCl sample did not exhibit any significant loss of photocatalytic activity after the third cycle of repeated testing for photocatalytic reduction of CO_2. An interesting phenomenon was observed in the process of CO_2 reduction in aqueous solution: The white BiOCl sample in the solution gradually became grey and then grey-black during the light irradiation. However, it became white again in aqueous solution after 2 days. Thus, we propose that a disproportionation reaction of Bi^{3+} to Bi^0 and Bi^{3+x} occurred under UV–visible light irradiation. This may be responsible for the recovery of the BiOCl nanoplates: The Bi^0 (grey), Bi^{3+x} and oxygen vacancies were produced by light irradiation, but the Bi^0 (grey) became reoxidized to Bi^{3+} (white) by the Bi^{3+x} and O_2 (since Bi^{3+x} is unstable in aqueous solution). In order to confirm both this assumption and the role of oxygen vacancies in the photoreduction of CO_2, the as-prepared BiOCl nanoplates and BiOCl-LT sample were characterized carefully.

3.3 Structure and morphology of BiOCl and BiOCl–LT nanoplates

TEM, high-resolution TEM (HRTEM) micrographs and selected area electron diffraction (SAED) pattern taken from an individual BiOCl nanoplate are represented in Figs. 3(a)–3(d). Figure S1 (in the ESM) also shows several BiOCl nanoplates with a width of about 50–200 nm and thickness of ~10 nm. The HRTEM micrograph (Fig. 3(b)) reveals clearly lattice fringes with a lattice spacing of 0.275 nm that is consistent with the (110) planes of the tetragonal

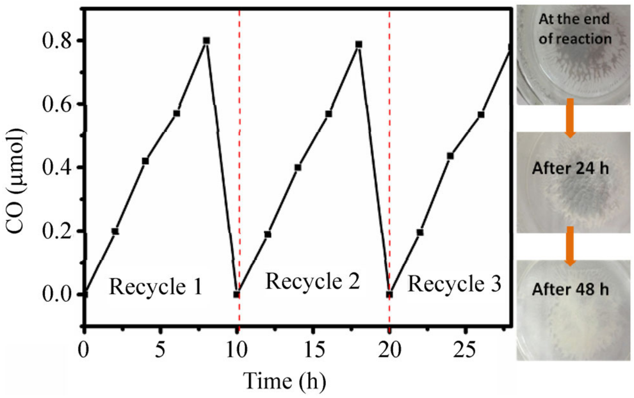

Figure 2 Cycling curve of photocatalytic production of CO on the BiOCl nanoplates.

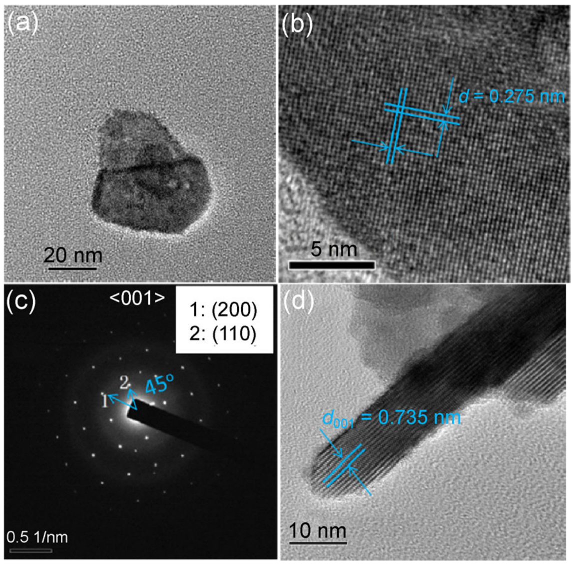

Figure 3 (a) TEM images for as-prepared BiOCl nanostructures; (b) HRTEM images for as-prepared BiOCl nanoplate; (c) SAED pattern of the BiOCl nanoplates (shown in (b)) and (d) HRTEM image of an as-prepared BiOCl nanoplate.

system of BiOCl, while the HRTEM (Fig. 3(d)) shows a lattice spacing of 0.735 nm that agrees well with the spacing of the (001) planes of tetragonal BiOCl. The SAED pattern in the inset of Fig. 3(c) was taken on a typical individual nanoplate (Fig. 3(b)), and shows that the nanoplate is single crystalline in nature. The angle between adjacent spots labeled in the SAED pattern is 45°, which is identical to the theoretical value of the angle between the (110) and (200) planes of tetragonal BiOCl [24]. According to the above results and the symmetry of tetragonal BiOCl, it is confirmed that the {001} facets are the preferentially exposed facets of the as-prepared BiOCl nanoplates.

The HRTEM images of BiOCl-LT show that the surfaces of BiOCl became disordered after light irradiation, where the disordered outer layer is ~1 nm in thickness, but on the inside there is good crystallinity (see Fig. S2, in the ESM). The crystal structures of the as-prepared samples were confirmed by XRD. As shown in Fig. 4(b), the XRD pattern could be well indexed to the tetragonal phase of BiOCl with the lattice parameters of $a = b = 0.3891$ nm and $c = 0.7369$ nm (JCPDS No. 06-249) and reveals that all the samples are well crystallized. After light irradiation, the white BiOCl sample became grey and black. A new peak (at 27.78°) appeared in the XRD pattern, which is characteristic of $BiO_{1.8}\cdot 0.04H_2O$ (JCPDS No. 540344). It is suggested that the Bi^{3+} may be oxidized to Bi^{3+x} by the photogenerated holes formed under irradiation by light. Other defects such as oxygen vacancies and bismuth vacancies may be produced at the same time, but they were not observed in the XRD pattern (since the levels of newly-formed substances may be below the detection limit of XRD (~5 at.%)).

3.4 Identification of oxygen vacancies and other defects formed in BiOCl-LT nanoplates.

Raman and XPS analysis were carried out to identify the photoinduced defects in the BiOCl-LT nanoplates. Photoinduced Bi vacancies on BiOCl-LT nanoplates were observed in Raman spectra (Fig. 5(a)). Compared with BiOCl nanoplates, there are two new bands at 69 and 98 cm^{-1}. These two new bands can be assigned to first-order vibration modes E_g and A_{1g} of Bi metal [25–27], confirming the presence of a very small

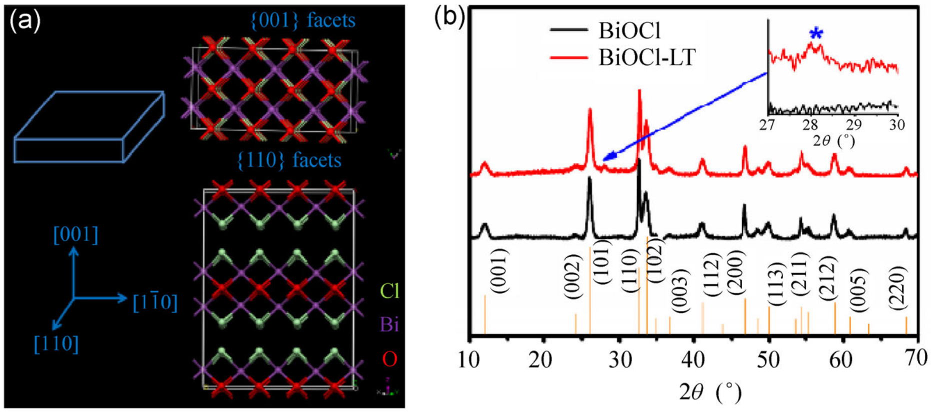

Figure 4 (a) Schematic illustration of the BiOCl structure. Perspective view of BiOCl; red balls: O, green balls: Cl, purple balls: Bi. (b) XRD patterns of as-prepared BiOCl nanoplates and BiOCl-LT nanoplates.

amount of Bi deposited on the surface. To further confirm the valency of bismuth and oxygen, XPS analysis was also carried out. As shown in Fig. 5(b), the two strong peaks in the Bi region at 159.1 and 164.4 eV can be respectively assigned to Bi $4f_{7/2}$ and Bi $4f_{5/2}$. The splitting between these bands is 5.3 eV, which is characteristic of BiOCl. For the BiOCl-LT sample, however, deconvolution suggests there are additional lower binding energy peaks at 160.3 and 157.2 eV; these are indicative of Bi centers with a lower valency, which can be attributed to the presence of oxygen vacancies [25]. There are also peaks with higher binding energies at 162.5 and 165.6 eV which can be attributed to Bi^{3+x} ions [28, 29]. These results suggest that BiOCl-LT contains Bi^0, Bi^{3+} and Bi^{3+x}. The high-resolution O 1s XPS spectra of the as-prepared BiOCl and BiOCl–LT samples are presented in Fig. 5(c), respectively. Both profiles are asymmetric and can be fitted to two Gaussian features, which are normally assigned as the low binding energy component (LBEC) and the high binding energy component (HBEC), indicating the presence of two different kinds of O species in the sample. The LBEC and HBEC can be attributed to the lattice oxygen and chemisorbed oxygen caused by the surface chemisorbed species such as hydroxyl and H_2O, respectively [30]. It has been previously reported that the HBEC component increases with the increase in the number of oxygen vacancies, and can lead to the asymmetry of the main peak [30, 31]. The high-resolution O 1s XPS spectra indicate that the peak area of HBEC is obviously larger in the BiOCl-LT sample as compared to the BiOCl sample. Moreover, the calculated ratios of the adsorbed oxygen to the lattice oxygen are 0.91 and 2.11 for the as-prepared BiOCl and BiOCl-LT, respectively, which strongly suggests the presence of a significant amount of oxygen deficiencies in the light-treated sample.

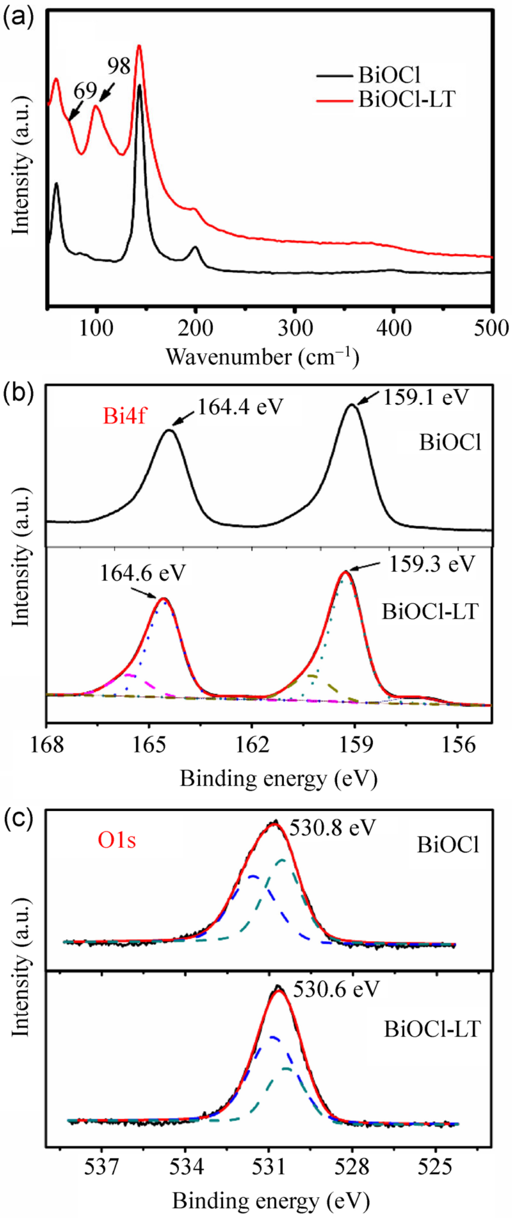

Figure 5 (a) Raman spectra of BiOCl and BiOCl-LT nanoplates; XPS spectra of (b) the Bi4f region and (c) the O1s region for BiOCl and BiOCl-LT nanoplates.

Oxygen vacancies can form an oxygen vacancy state lying close to the conduction band of the photocatalyst, which results in the absorption of visible light [32, 33]. Figure 6(a) shows the DRS spectra of the as-prepared BiOCl and BiOCl-LT samples. The BiOCl nanoplates do not have any absorption in the visible light range. After light irradiation to give BiOCl-LT, absorption in the visible light range increased. This reveals that oxygen vacancies (V_O) emerged after light irradiation. Furthermore, Fig. 6(b) shows the difference between the PL spectra of BiOCl and BiOCl-LT. For BiOCl, there is a main band at 365 nm (3.34 eV). Because the energy of this photoluminescence is nearly equal to the band gap (3.5 eV) of bulk BiOCl, this emission is attributed to the recombination of free electrons from the bottom of the conduction band to the recombination

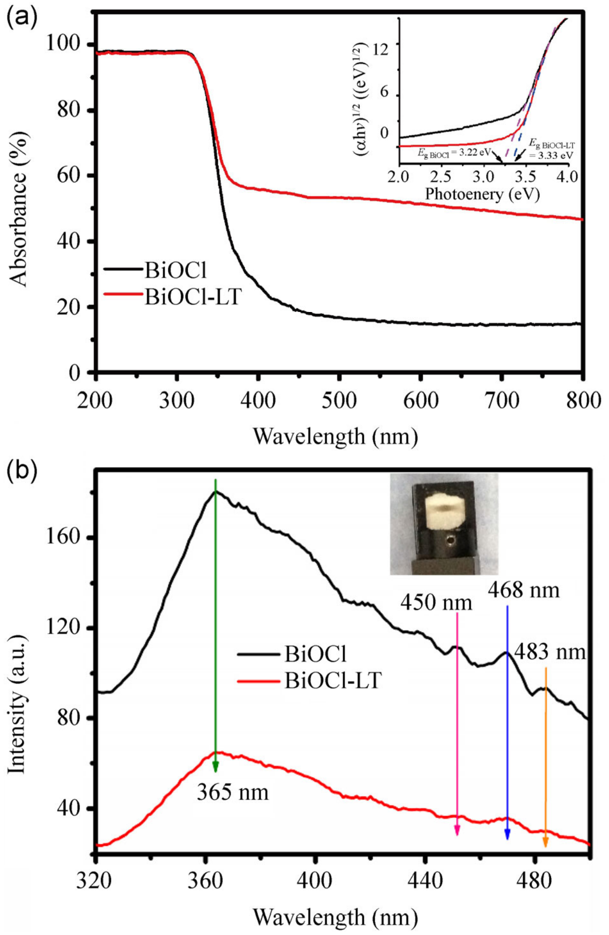

Figure 6 (a) UV–visible diffuse reflectance spectra of BiOCl and BiOCl-LT nanoplates. Inset: The bandgap value, estimated from a plot of $(\alpha h\nu)^{1/2}$ versus photon energy. (b) PL spectra of BiOCl and BiOCl-LT nanoplates.

center in the ground state. It is worth noting that, different from the reported spectrum of pure BiOCl [34], there are several additional absorption bands at 450, 468 and 483 nm. These bands may relate to the $V_O^{\cdot\cdot}$, isolated V_{Bi}''' defects and triple vacancy associates $'''V_{Bi}V_O^{\cdot\cdot}V_{Bi}'''$ formed *in situ*. It was observed that the thin BiOCl nanoplates were "damaged" (became to grey and black) by the light (280 nm) in the photoluminescence spectrometer (see the inset of Fig. 6(b)). The photoinduced electrons in defects states recombine with photoinduced holes in the ground state and cause the new photoluminescence bands. For the BiOCl-LT sample, all the absorption bands became weaker. A weaker PL intensity implies a lower recombination rate of the electrons and holes under light irradiation [34, 35].

3.5 Mechanism of the formation of vacancies and their role in CO_2 photoreduction

The mechanism of formation of the oxygen vacancies and bismuth vacancies is closely related to the crystal structure of BiOCl and is schematically illustrated in Scheme 1. According to the results in Fig. 3 and the symmetry of BiOCl, the bottom and top surfaces of the BiOCl nanoplates are terminated {001} facets, while the side surfaces are {110} facets. The atomic structures of the {001} facets are shown in Fig. 4(a). Under photochemical conditions, the surface atoms can escape from the lattice more easily than the inner atoms [25, 36]. In the crystal structure of BiOCl, the Bi atoms in the $[Bi_2O_2]^{2+}$ layers are exposed on the outside while the O atoms are buried inside (as seen in Fig. 4(a)), which means that the Bi atoms should escape from the lattice more easily than the inner atoms and results in the predominant defects in the BiOCl nanoplates being isolated V_{Bi}'''. This hypothesis was verified by the XPS and Raman analysis. On the other hand, BiOCl with exposed {001} facets has a high density of surface O atoms and a small formation energy [37]. This means that the $V_O^{\cdot\cdot}$ could easily be formed on these facets to balance the electron charge in the crystal.

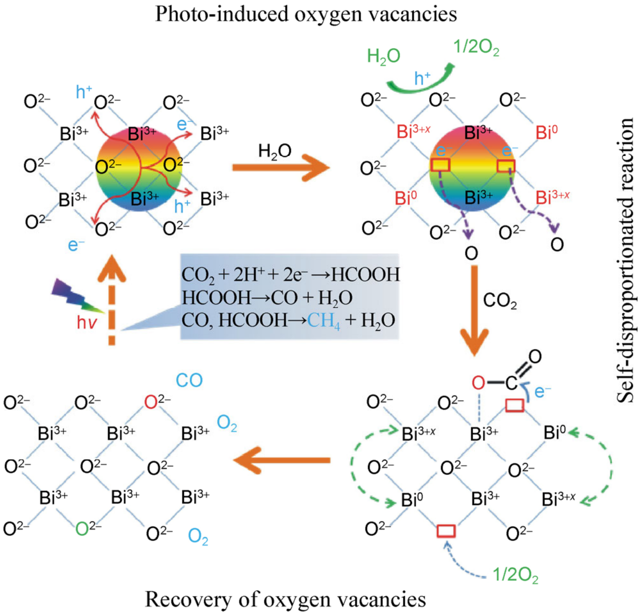

Scheme 1 Possible reaction pathways for the formation of CO, CH_4 and O_2 from CO_2 photoreduction with H_2O on BiOCl nanoplates.

These defects in the BiOCl nanoplates supplied the active sites for the photoreduction of the CO_2. It has been reported that an oxygen vacancy on the surface can preferentially trap CO_2 molecules [4]. The FTIR spectra in Fig. 7 provide information about interaction between CO_2 and the BiOCl nanoplates. As shown in Figs. 7(a) and 7(b), IR bands at 3,100–3,600 and ~1,637 cm^{-1} can be assigned to the stretching vibrations of OH groups and physically adsorbed H_2O, respectively [38]. The weak IR bands at 1,410–1,490 and 1,500–1,590 cm^{-1} may assigned to the bicarbonate (HCO_3^-) features and mono- and bidentate carbonates (b-CO_3^{2-}, m-CO_3^{2-}), respectively [4]. By contrast, after light irradiation, the IR bands at 3,100–3,600 cm^{-1} disappeared or became significantly weakened, probably because the H_2O molecules were consumed or replaced by other molecules. The significantly reduced intensities of the bands at 1,400–1,700 cm^{-1} can be attributed to the reduction of Bi^{3+} to Bi^0 and the weak interactions between the reduced bismuth atoms and the carbonyl oxygen atoms. Meanwhile, new bands appeared at 2,351 cm^{-1} (as shown in Fig. 7(c)), which were assigned to CO adsorbed on Bi^0 surface [39]. The results are in good agreement with earlier FTIR results obtained by Martins et al. [40] and Koper et al. [39], in particular in evidencing the formation of surface-adsorbed CO species on Bi. This provides evidence that the photoexcited electrons trapped in the defect sites can be transferred to the CO_2 adsorbed on the surface of BiOCl nanoplates, although the literature indicates that the one-electron reduction of CO_2 is very difficult or impossible [41, 42]. Recently, Zhang et al. reported that the (001) surface of BiOCl preferentially reduces O_2 to $O^{2-\cdot}$ through a one-electron transfer assisted by the situ-generated oxygen vacancy [26]. This suggests that the oxygen vacancy promotes the one-electron transfer reaction. Thus, the activated CO_2 gained the photogenerated electron and released a carbon monoxide molecule, consuming a surface oxygen vacancy (the oxygen atom filled the site of the oxygen vacancy). However, these O atoms will easily escape from the lattice again under light irradiation and the oxygen vacancy formed again (see the Experimental section). In addition, the photogenerated holes will oxidize H_2O to produce O_2. This process results in a very high ratio of O_2/CO, in agreement with the experimental observations.

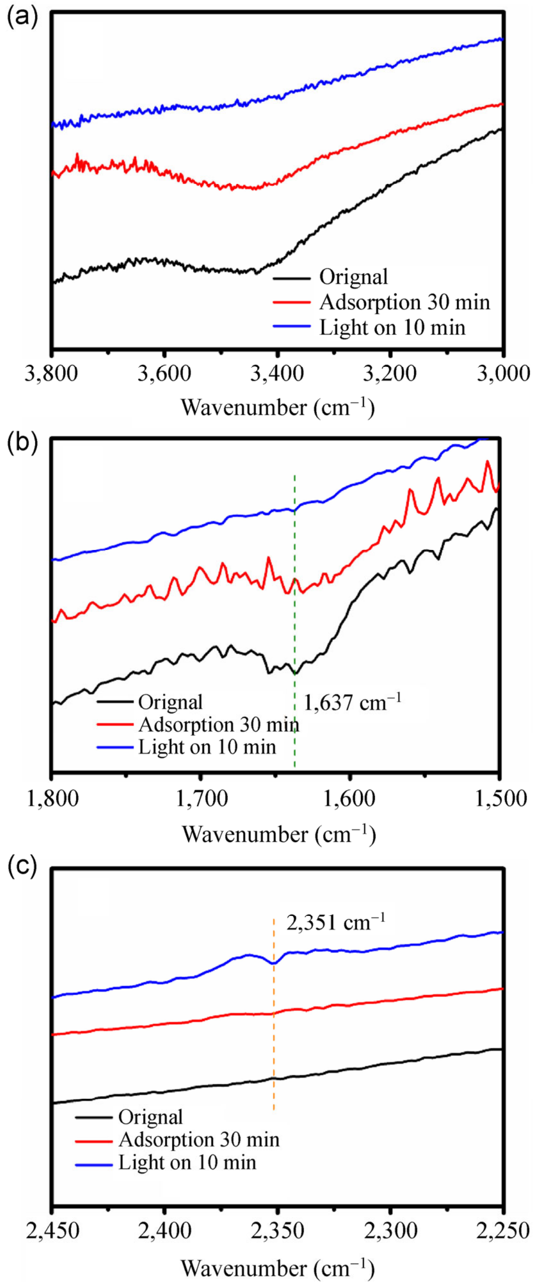

Figure 7 FTIR spectra after interaction of CO_2 and H_2O with BiOCl nanoplates: (a) 3,000–3,800 cm^{-1}; (b) 1,500–1,800 cm^{-1}; (c) 2,250–2,450 cm^{-1}. The light was turned on after the samples sat in the dark for 30 min to undergo adsorption.

On the other hand, we propose that the CH_4 formed may come from the carbon-containing intermediates such as CO, surface HCO_3^- and HCOOH which are converted to CH_4 via a multi-electron transfer process using the available protons (in water) [5]. It is also possible for CH_4 to decompose through reaction with photogenerated ·OH radicals to form CO. In Fig. 1(a), an obvious decrease in the amount of CH_4 at 6 h suggested that it was consumed in the process of CO formation. These two factors may contribute to the low yield of CH_4 observed in this work.

4 Conclusion

This work presents a novel approach to fabricate regenerable oxygen vacancies on a BiOCl nanoplate photocatalyst for the reduction of CO_2 to CO and CH_4. Oxygen vacancies are readily formed since the surface O atoms are exposed, and CO_2 molecules can be trapped on these oxygen vacancies on the surface of BiOCl nanoplates. The reduction process is to a large extent associated with the reversible formation of surface oxygen vacancies, which provide not only the sites for the adsorption of oxygen atoms from CO_2 but also effectively separate the photoinduced electron–hole pairs. The regeneration of oxygen vacancies is realized during the CO_2 photocatalytic reduction in water irradiated by a Xe lamp. Our results provide some new insights into an in-depth understanding of defect-dependent photocatalytic properties. This work may open up a new avenue for the design of photocatalysts with high solar-driven photocatalytic performance by engineering the intrinsic defects on the surface.

Acknowledgements

This work was supported by the National Basic Research Program of China (No. 2013CB933203) and the National Natural Science Foundation of China (Nos. 51272303 and 50972155).

Electronic Supplementary Material: Supplementary material (further details of TEM images of BiOCl-LT sample, band structure information, photocatalytic reduction of CO_2 under different conditions) is available in the online version of this article at http://dx.doi.org/10.1007/s12274-014-0564-2.

References

[1] Sakakura, T.; Choi, J. C.; Yasuda, H. Transformation of carbon dioxide. *Chem. Rev.* **2007**, *107*, 2365–2387.

[2] Appel, A. M.; Bercaw, J. E.; Bocarsly, A. B.; Dobbek, H.; DuBois, D. L.; Dupuis, M.; Ferry, J. G.; Fujita, E.; Hille, R.; Kenis, P. J. A. et al. Frontiers, opportunities, and challenges in biochemical and chemical catalysis of CO_2 fixation. *Chem. Rev.* **2013**, *113*, 6621–6658.

[3] Izumi, Y. Recent advances in the photocatalytic conversion of carbon dioxide to fuels with water and/or hydrogen using solar energy and beyond. *Coord. Chem. Rev.* **2013**, *257*, 171–186.

[4] Liu, L. J.; Zhao, H. L.; Andino, J. M.; Li, Y. Photocatalytic CO_2 reduction with H_2O on TiO_2 nanocrystals: Comparison of anatase, rutile, and brookite polymorphs and exploration of surface chemistry. *ACS Catal.* **2012**, *2*, 1817–1828.

[5] Wang, W. N.; An, W. J.; Ramalingam, B.; Mukherjee, S.; Niedzwiedzki, D. M.; Gangopadhyay, S.; Biswas, P. Size and structure matter: Enhanced CO_2 photoreduction efficiency by size-resolved ultrafine Pt nanoparticles on TiO_2 single crystals. *J. Am. Chem. Soc.* **2012**, *134*, 11276–11281.

[6] Mahmodi, G.; Sharifnia, S.; Rahimpour, F.; Hosseini, S. N. Photocatalytic conversion of CO_2 and CH_4 using ZnO coated mesh: Effect of operational parameters and optimization. *Sol. Energy Mater. Sol. Cell.* **2013**, *111*, 31–40.

[7] Gokon, N.; Hasegawa, N.; Kaneko, H.; Aoki, H.; Tamaura, Y.; Kitamura, M. Photocatalytic effect of ZnO on carbon gasification with CO_2 for high temperature solar thermochemistry. *Sol. Energy Mater. Sol. Cell.* **2003**, *80*, 335–341.

[8] Liu, Q.; Zhou, Y.; Tian, Z. P.; Chen, X. Y.; Gao, J.; Zou, Z. G. Zn_2GeO_4 crystal splitting toward sheaf-like, hyperbranched nanostructures and photocatalytic reduction of CO_2 into CH_4 under visible light after nitridation. *J. Mater. Chem.* **2012**, *22*, 2033–2038.

[9] Li, X.; Liu, H. L.; Luo, D. L.; Li, J. T.; Huang, Y.; Li, H. L.; Fang, Y. P.; Xu, Y. H.; Zhu, L. Adsorption of CO_2 on heterostructure $CdS(Bi_2S_3)/TiO_2$ nanotube photocatalysts and their photocatalytic activities in the reduction of CO_2 to methanol under visible light irradiation. *Chem. Eng. J.* **2012**, *180*, 151–158.

[10] Praus, P.; Kozák, O.; Kočí, K.; Panáček, A.; Dvorský, R. CdS nanoparticles deposited on montmorillonite: Preparation, characterization and application for photoreduction of carbon dioxide. *Colloid Interface Sci.* **2011**, *360*, 574–579.

[11] Cheng, H. F.; Huang, B. B.; Liu, Y. Y.; Wang, Z. Y.; Qin, X. Y.; Zhang, X. Y.; Dai, Y. An anion exchange approach to Bi_2WO_6 hollow microspheres with efficient visible light photocatalytic reduction of CO_2 to methanol. *Chem. Commun.* **2012**, *48*, 9729–9731.

[12] Zhou, Y.; Tian, Z. P.; Zhao, Z. Y.; Liu, Q.; Kou, J. H.; Chen, X. Y.; Gao, J.; Yan, S. C.; Zou, Z. G. High-yield synthesis of ultrathin and uniform Bi_2WO_6 square nanoplates benefitting from photocatalytic reduction of CO_2 into renewable hydrocarbon fuel under visible light. *ACS Appl. Mater. Interfaces* **2011**, *3*, 3594–3601.

[13] Liu, Y. Y.; Huang, B. B.; Dai, Y.; Zhang, X. Y.; Qin, X. Y.; Jiang, M. H.; Whangbo, M. H. Selective ethanol formation from photocatalytic reduction of carbon dioxide in water with $BiVO_4$ photocatalyst. *Catal. Commun.* **2009**, *11*, 210–213.

[14] Iizuka, K.; Wato, T.; Miseki, Y.; Saito, K.; Kudo, A. Photocatalytic reduction of carbon dioxide over Ag cocatalyst-loaded $A\text{La}_4\text{Ti}_4\text{O}_{15}$ (A = Ca, Sr, and Ba) using water as a reducing reagent. *J. Am. Chem. Soc.* **2011**, *133*, 20863–20868.

[15] Liu, C.; Dubois, K. D.; Louis, M. E.; Vorushilov, A. S.; Li, G. H. Photocatalytic CO_2 reduction and surface immobilization of a tricarbonyl Re(I) compound modified with amide groups. *ACS Catal.* **2013**, *3*, 655–662.

[16] Lo, L. T. L.; Lai, S. W.; Yiu, S. M.; Ko, C. C. A new class of highly solvatochromic dicyano rhenate(I) diimine complexes—synthesis, photophysics and photocatalysis. *Chem. Commun.* **2013**, *49*, 2311–2313.

[17] Morimoto, T.; Tanabe, J.; Sakamoto, K.; Koike, K.; Ishitani, O. Selective H_2 and CO production with rhenium(I) biscarbonyl complexes as photocatalyst. *Res. Chem. Intermed.* **2013**, *39*, 437–447.

[18] Wang, G. M.; Ling, Y. C.; Li, Y. Oxygen-deficient metal oxide nanostructures for photoelectrochemical water oxidation and other applications. *Nanoscale* **2012**, *4*, 6682–6691.

[19] Jiao, W.; Wang, L. Z.; Liu, G.; Lu, G. Q.; Cheng, H. M. Hollow anatase TiO_2 single crystals and mesocrystals with dominant {101} facets for improved photocatalysis activity and tuned reaction preference. *ACS Catal.* **2012**, *2*, 1854–1859.

[20] Liu, L. J.; Zhao, C. Y.; Li, Y. Spontaneous dissociation of CO_2 to CO on defective surface of Cu(I)/TiO_{2-x} nanoparticles at room temperature. *J. Phys. Chem. C* **2012**, *116*, 7904–7912.

[21] Ye, L. Q.; Deng, K. J.; Xu, F.; Tian, L. H.; Peng, T. Y.; Zan, L. Increasing visible-light absorption for photocatalysis with black BiOCl. *Phys. Chem. Chem. Phys.* **2012**, *14*, 82–85.

[22] Ye, L. Q.; Zan, L.; Tian, L. H.; Peng, T. Y.; Zhang, J. J. The {001} facets-dependent high photoactivity of BiOCl nanosheets. *Chem. Commun.* **2011**, *47*, 6951–6953.

[23] Guan, M. L.; Xiao, C.; Zhang, J.; Fan, S. J.; An, R.; Cheng, Q. M.; Xie, J. F.; Zhou, M.; Ye, B. J.; Xie, Y. Vacancy associates promoting solar-driven photocatalytic activity of ultrathin bismuth oxychloride nanosheets. *J. Am. Chem Soc.* **2013**, *135*, 10411–10417.

[24] Wang, D. H.; Gao, G. Q.; Zhang, Y. W.; Zhou, L. S.; Xu, A. W.; Chen, W. Nanosheet-constructed porous BiOCl with dominant {001} facets for superior photosensitized degradation. *Nanoscale* **2012**, *4*, 7780–7785.

[25] Weng, S. X.; Chen, B. B.; Xie, L. Y.; Zheng, Z. Y.; Liu, P. Facile *in situ* synthesis of a Bi/BiOCl nanocomposite with high photocatalytic activity. *J. Mater. Chem A* **2013**, *1*, 3068–3075.

[26] Zhao, K.; Zhang, L. Z.; Wang, J. J.; Li, Q. X.; He, W. W.; Yin, J. J. Surface structure-dependent molecular oxygen activation of BiOCl single-crystalline nanosheets. *J. Am. Chem Soc.* **2013**, *135*, 15750–15753.

[27] Liu, X. W.; Cao, H. Q.; Yin, J. F. Generation and photocatalytic activities of Bi@Bi_2O_3 microspheres. *Nano Res.* **2011**, *4*, 470–482.

[28] Zhang, S. M.; Zhang, G. K.; Yu, S. J.; Chen, X. G.; Zhang, X. Y. Efficient photocatalytic removal of contaminant by $Bi_3Nb_xTa_{1-x}O_7$ nanoparticles under visible light irradiation. *J. Phys. Chem. C* **2009**, *113*, 20029–20035.

[29] Jovalekic, C.; Pavlovic, M.; Osmokrovic, P.; Atanasoska, L. X-ray photoelectron spectroscopy study of $Bi_4Ti_3O_{12}$ ferroelectric ceramics. *Appl. Phys. Lett.* **1998**, *72*, 1051–1053.

[30] Xing, M. Y.; Fang, W. Z.; Nasir, M.; Ma, Y. F.; Zhang, J. L.; Anpo, M. Self-doped Ti^{3+}-enhanced TiO_2 nanoparticles with a high-performance photocatalysis. *J. Catal.* **2013**, *297*, 236–243.

[31] Armelao, L.; Bottaro, G.; Maccato, C.; Tondello, E. Bismuth oxychloride nanoflakes: Interplay between composition–structure and optical properties. *Dalton Trans.* **2012**, *41*, 5480–5485.

[32] Aiura, Y.; Iga, F.; Nishihara, Y.; Ohnuki, H.; Kato, H. Effect of oxygen vacancies on electronic states of $CaVO_{3-\delta}$ and $SrVO_{3-\delta}$: A photoemission study. *Phys. Rev. B* **1993**, *47*, 6732–6735.

[33] Zhang, X. C.; Zhao, L. J.; Fan, C. M.; Liang, Z. H.; Han, P. D. Effects of oxygen vacancy on the electronic structure and absorption spectra of bismuth oxychloride. *Comp. Mater. Sci.* **2012**, *61*, 180–184.

[34] Deng, Z. T.; Tang, F. Q.; Muscat, A. J. Strong blue photoluminescence from single-crystalline bismuth oxychloride nanoplates. *Nanotechnology* **2008**, *19*, 295705.

[35] Wang, J. P.; Wang, Z. Y.; Huang, B. B.; Ma, Y. D.; Liu, Y. Y.; Qin, X. Y.; Zhang, X. Y.; Dai, Y. Oxygen vacancy induced band-gap narrowing and enhanced visible light photocatalytic activity of ZnO. *ACS Appl. Mater. Interfaces* **2012**, *4*, 4024–4030.

[36] Li, Y. X.; Zang, L.; Li, Y.; Liu, Y.; Liu, C. Y.; Zhang, Y.; He, H. Q.; Wang, C. Y. Photoinduced topotactic growth of bismuth nanoparticles from bulk $SrBi_2Ta_2O_9$. *Chem. Mater.* **2013**, *25*, 2045–2050.

[37] Zhang, H. J.; Liu, L.; Zhou, Z. First-principles studies on facet-dependent photocatalytic properties of bismuth oxyhalides (BiOXs). *RSC Adv.* **2012**, *2*, 9224–9229.

[38] Tang, J. L.; Zhao, H. P.; Li, G. F.; Lu, Z.; Xiao, S. Q.; Chen, R. Citrate/urea/solvent mediated self-assembly of $(BiO)_2CO_3$ hierarchical nanostructures and their associated photocatalytic performance. *Ind. Eng. Chem. Res.* **2013**, *52*, 12604–12612.

[39] Kwon, Y.; Birdja, Y.; Spanos, I.; Rodriguez, P.; Koper, M. T. M. Highly selective electro-oxidation of glycerol to dihydroxyacetone on platinum in the presence of bismuth. *ACS Catal.* **2012**, *2*, 759–764.

[40] Martins, C. A.; Giz, M. J.; Camara, G. A.; Generation of carbon dioxide from glycerol: Evidences of massive production on polycrystalline platinum. *Electrochim. Acta* **2011**, *56*, 4549–4553.

[41] Indrakanti, V. P.; Kubicki, J. D.; Schobert, H. H. Photoinduced activation of CO_2 on Ti-based heterogeneous catalysts: Current state, chemical physics-based insights and outlook. *Energy Environ. Sci.* **2009**, *2*, 745–758.

[42] Dimitrijevic, N. M.; Vijayan, B. K.; Poluektov, O. G.; Rajh, T.; Gray, K. A.; He, H. Y.; Zapol, P. Role of water and carbonates in photocatalytic transformation of CO_2 to CH_4 on titania. *J. Am. Chem. Soc.* **2011**, *133*, 3964–3971.